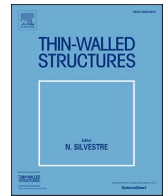


# ULRR

## Morphing of symmetric cross-ply cylindrical shells by minimising the brazier moment: Optimised hinge folding

Item Type	Article
Authors	Bowen, Aileen G.;Zucco, Giovanni;Weaver, Paul M.
Citation	Thin-Walled Structures;158, 107122
Publisher	Elsevier
Download date	2026-06-13 08:51:56
Item License	<a href="https://creativecommons.org/licenses/by-nc-sa/1.0/">https://creativecommons.org/licenses/by-nc-sa/1.0/</a>
Link to Item	<a href="https://hdl.handle.net/10344/9689">https://hdl.handle.net/10344/9689</a>



# Morphing of symmetric cross-ply cylindrical shells by minimising the Brazier moment: Optimised hinge folding

Aileen G. Bowen<sup>a,\*</sup>, Giovanni Zucco<sup>a</sup>, Paul M. Weaver<sup>b</sup>

<sup>a</sup> University of Limerick and Bernal Institute, Ireland

<sup>b</sup> Bernal Chair in Composite Materials and Structures, University of Limerick, Ireland

## ARTICLE INFO

### Keywords:

Flexible hinges  
Brazier effect  
Deployable and folding structures  
Brazier moment minimisation  
Cross-ply flexible hinge  
Thin-walled tubes under bending

## ABSTRACT

Aerospace and industries where both localised compliance and weight savings play a central role in design can benefit from using flexible hinges. These morphing structures use no mechanical hinges for folding. They fold by exploiting the limit point, i.e. the Brazier moment, of a geometrically nonlinear structural response characteristic of thin-walled beams under bending. Therefore, a smaller Brazier moment induces smaller non-classical stresses in the hinge during folding.

Two aspects make cross-ply laminates attractive for designing flexible hinges. Firstly, the difference between the Brazier moment of an optimal symmetric generic laminate and that of an optimal symmetric cross-ply is relatively small. Secondly, cross-ply laminates do not exhibit extension-shear or bend-twist couplings which can induce complex deformations which can present challenges during design, especially considering that available analytical solutions of the Brazier moment neglect their effects. Driven by these premises, this work contributes to the preliminary design of flexible hinges by offering an analytical solution of the optimum symmetric cross-ply laminate for minimising the Brazier moment, which is subsequently validated through geometrically nonlinear finite element analysis. Moreover, this work provides insights into the prediction of the folding load considering the effects of local buckling instabilities.

## 1. Introduction

Structures in Nature are able to temporally change their shape to accomplish a broad variety of functions using their intrinsic structural properties. For example, seed-bearing pine cones disperse their seeds by changing from a close to an open configuration as a response to humidity changes. They achieve such shape morphing thanks to the composite anisotropic nature of their structure [1]. The multi-functional ability of Nature to change shape has not been yet fully exploited by engineered-structures. Shape-adaptive, i.e. morphing, engineered-structures attempt to eradicate this shortcoming. Their potential applications include diverse engineering fields such as aerospace [2], automobile [3] and wind energy [4]. Flexible hinges belong to a vast subfield of morphing structures known as deployables [5] with applications including deployable booms for aerospace applications [6–8], see Fig. 1, and the concept of a deployable wing by Lachenal et al. [9].

Flexible hinges based on the Brazier effect make use of localised compliance derived from nonlinear elastic deformations. In comparison

with conventionally hinged deployable structures, flexible hinges enable the design of lighter structures with smaller part count and eliminate the need for lubrication. These benefits, desirable in many engineering applications, originate from the omission of mechanical linkages thanks to a nonlinear structural response often known as the Brazier effect [10, 11]. The Brazier effect can be understood by considering a circular tube under bending load,  $M$ , that not only changes its axial curvature,  $\kappa$ , but also its circumferential curvature, i.e its cross-section flattens, see Fig. 2. Increasing the flattening of the cross-section steadily decreases the circular tube's bending stiffness until the limit point,  $(\kappa_{Brz}, M_{Brz})$  - point C in Fig. 2 - is reached, when the structure exhibits unstable behaviour and folds. Then, lower  $M_{Brz}$  translates to a lower folding load for the hinge, and therefore, lower stresses induced by folding.

Layered composite materials offer both layup and material properties as design parameters to minimise the folding load of a hinge. Considering that both axial and circumferential curvature changes take place, the optimum stacking sequence for minimising  $M_{Brz}$  could be considered to comprise longitudinal (zero degree) and circumferential (90°) plies of stacking sequence to be established. Herein, this hypothesis is analysed in some detail.

\* Corresponding author.

E-mail addresses: [Aileen.BowenPerez@ul.ie](mailto:Aileen.BowenPerez@ul.ie) (A.G. Bowen), [Giovanni.Zucco@ul.ie](mailto:Giovanni.Zucco@ul.ie) (G. Zucco), [Paul.Weaver@ul.ie](mailto:Paul.Weaver@ul.ie) (P.M. Weaver).

<https://doi.org/10.1016/j.tws.2020.107122>

Received 19 June 2020; Received in revised form 12 August 2020; Accepted 27 August 2020

Available online 8 October 2020

0263-8231/© 2020 The Authors. Published by Elsevier Ltd. This is an open access article under the CC BY license (<http://creativecommons.org/licenses/by/4.0/>).

Symbols			
$A_{11}$	Longitudinal stiffness, $N/mm$	$x_i$	Volume fraction of the $i$ -th laminate layer
$A_{16}, A_{26}$	Extension-shear coupling stiffness, $N/mm$	$x_{1\ opt}$	Optimum volume fraction of 90-deg lamina in [0 90 0] laminate
$d$	Tube diameter, $mm$	$\chi$	Collapse parameter
$D_{16}, D_{26}$	Bend-twist coupling stiffness, $Nmm$	$\eta$	Cross-sectional flattening
$D_{22}$	Circumferential bending stiffness, $Nmm$	$\kappa$	Curvature, $1/mm$
$E_{\theta,z}$	Effective moduli for orthotropic laminates, $N/mm^2$	$\lambda_1$	First buckling load, $Nmm$
$E_{11}$	Longitudinal Young's modulus, $N/mm^2$	$\nu_{12}$	Poisson's ratio
$E_{22}$	Transverse Young's modulus, $N/mm^2$	$\bar{Q}_{11}, \bar{Q}_{22}$	Transformed stiffnesses, $N/mm^2$
$G_{12}$	Shear modulus, $N/mm^2$	$\phi_{x,y,z}$	Rotations against $x$ , $y$ and $z$ axes, $rad$
$K$	Coefficient of Brazier moment analytical solution	<i>Subscripts and superscripts</i>	
$L$	Tube length, $mm$	4 – ply	4-ply symmetric laminate
$M_{Brz}$	Brazier moment, $Nmm$	$E$	Elliptical cross-section
$m_{Brz}$	normalised Brazier moment	$H$	Harursampath and Hodges
$M_i$	FE instability load, $Nmm$	$K$	Kedward
$n$	Number of plies	$min$	minimum
$r$	Tube mid-surface radius, $mm$	$opt$	optimum
$t$	Thickness of the cylinder, $mm$	$S$	Stockwell and Cooper
$u_{x,y,z}$	Displacements in $x$ , $y$ and $z$ directions, $mm$	$T$	Tatting et al.
$U_1$	Material invariant, quasi-isotropic modulus		

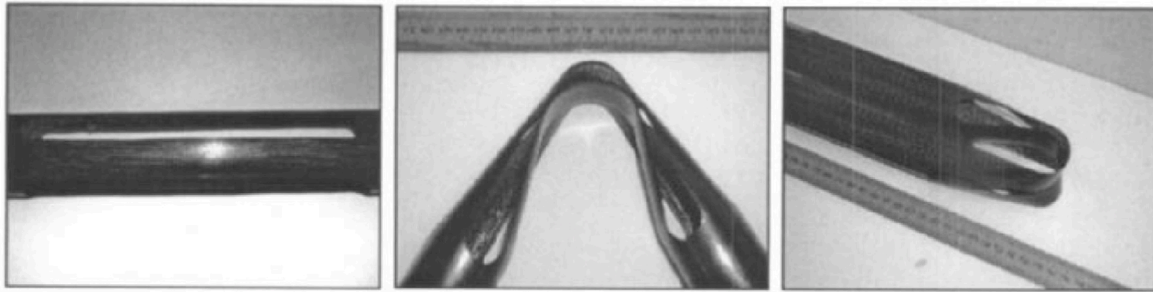


Fig. 1. Yee and Pellegrino's composite tube hinge deployed, partially folded and fully folded [7].

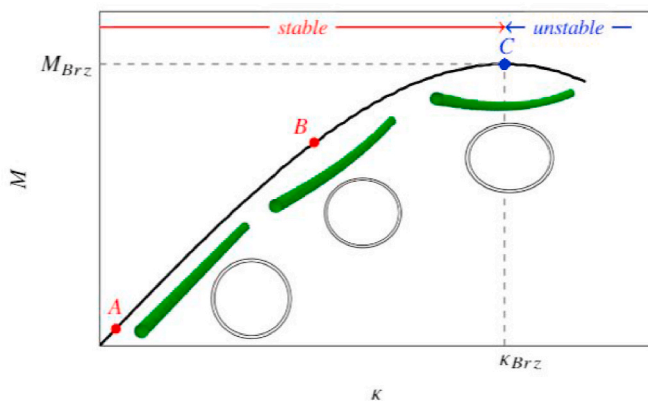


Fig. 2. Equilibrium curve of a circular thin-walled tube under bending.

Recently, Bowen et al. [12] studied the optimum laminate for the minimisation of  $M_{Brz}$  in long orthotropic circular tubes. Their results showed that the optimum laminate for minimising  $M_{Brz}$  is actually not cross-ply, as we intimated earlier, which incidentally it is for maximising  $M_{Brz}$  [13] with stacking sequence [90 0 90], and actually depends on material properties. Furthermore, their results show that the effects of extension-shear and bend-twist couplings in the minimisation analysis

are non-negligible.

Two main aspects make cross-ply laminates interesting candidates for the design of flexible hinges though. Firstly, as already described, is the attainable small difference in  $M_{Brz}$  between optimum symmetric cross-ply laminates and global 4-ply symmetric optimum laminates. Secondly, the design simplicity offered by the absence of extension-shear and bend-twist couplings is beneficial.

The folding of flexible hinges has captured less research interest than their opposite shape change, i.e. deployment. Lachenal et al. [9] studied folding in detail for the design of a deployable wing. They developed both finite element and analytical models to predict the folding load and deformation of the wing using an energetic model analogous to that from Brazier [11]. Even when the design of the wing included cut-outs (open cross-section), the analytical model captured the nonlinear bending nature of the problem which was further confirmed experimentally. Critical locations during folding were in the cut-out regions which acted as stress concentrators. Mallikarachchi and Pellegrino [14] also considered folding in the design of deployable booms. Cut-outs were also identified as critical locations, as a consequence their geometry was parametrically optimised. An alternative design approach minimises the folding load to reduce nominal stresses. Nevertheless, the design of such a structure is holistic; it does not depend solely on the packing process but also on all morphological changes (packing, deployment, locking and folding). All these factors influence design to various extents depending on the application under consideration. For

example, a minimum folding load could be a driving factor for applications whose main objective is once only folding, as could be required for transportation purposes before being deployed on site. In contrast, the minimum folding load would be less of a factor for applications where actuation is the main aim since the reduction of internal strain energy, depending on states of stresses and strains, is most important. Independent of application, analytical solutions that can be used simply to optimise morphological changes are important tools for multi-objective design.

The objective of this work is to design optimal elastic cross-ply flexible hinges providing detailed understanding of the folding (packing) process. In particular, we present an analytical solution which defines the optimum cross-ply laminate to minimise the folding load. In line with the objective of optimal folding, we provide an investigation on the mechanisms which can take place during folding, i.e. Brazier instability or local buckling. The outputs from this work are applicable to cross-ply cylindrical tubes with flexible hinges embedded in their structure where the tubes are sufficiently long so that the effect of boundary conditions can be neglected. To the best of the authors' knowledge no prior work considers optimal folding of cross-ply flexible hinges nor examines their potential advantages for design.

Additionally, this work is part of ongoing research to assess the use of flexible hinges for novel applications including the folding of large wind turbine blades to facilitate their transportation. Jensen et al. [15] showed that the Brazier effect also takes place in wind turbine blades, while Cecchini and Weaver offered an analytical solution of the Brazier moment for multibay airfoil sections [16]. However, few works appear to exploit the Brazier effect. The investigation of the minimisation of the Brazier moment in circular cross-sections offers, therefore, valuable insights which are potentially to some degree applicable to airfoil cross-sections.

This article is organised into four sections. The first section verifies, through numerical minimisation, that [0 90 0] is the optimal symmetric cross-ply stacking sequence. The minimisation also confirms the material dependency of the solution. The second section presents an analytical solution which defines the optimum volume fraction of [0 90 0] as a function of material properties. The analytical solution is validated through geometrically nonlinear Finite Element (FE) analysis using the Riks arc-length algorithm in Abaqus [17]. Results from the analytical solution do not directly deliver the magnitude of the minimum Brazier moment,  $M_{Brz, min}$ . In fact, the prediction of this magnitude depends on the analytical solution chosen by the designer. To guide the designer in this choice, the third section offers a comparison of analytical solutions [18–21] against numerical results obtained through geometrically nonlinear FE analysis.

Stresses originating on the compressive side of the tube during bending induce local buckling which could precede the Brazier instability. The last section is dedicated to the prediction of which type of instability causes unstable behaviour of the hinge, i.e. Brazier instability or local buckling. For this purpose, the use of a parameter defining the critical instability proposed by Tatting et al. [21] is considered. Furthermore, based on numerical FE results additional insights to the prediction of the instability mode are provided.

**2. Numerical minimisation**

The Brazier moment,  $M_{Brz}$ , of a circular orthotropic tube of infinite length under pure bending has been analytically determined by several authors to be given by

$$M_{Brz} = K \cdot r \cdot \sqrt{A_{11} D_{22}} \tag{1}$$

where  $K$  is a constant differing by author,  $K = 3.42, \pi$  or  $4.22$  according to Kedward [18], Stockwell and Cooper [19] or Harursampath and Hodges [20], respectively. No satisfactory explanations for these differences have yet been offered but arise due to differing kinematic

**Table 1**  
Material properties of sample materials.

Material	$E_{11}$ [GPa]	$E_{22}$ [GPa]	$G_{12}$ [GPa]	$\nu_{12}$
1	181	10.27	7.17	0.28
2	135	7.5	5	0.30
3	38.6	8.27	4.14	0.26
4	53.8	17.9	8.96	0.25

**Table 2**  
Minimisation results for tubes made of sample materials.

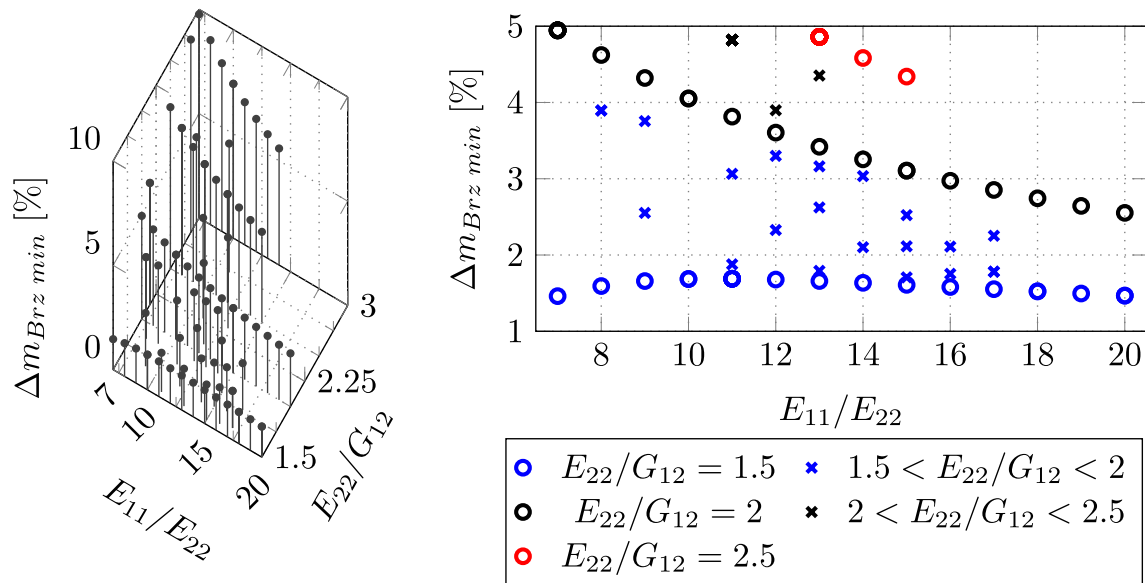
Material	Number of plies	Stacking Sequence	$x_i^{opt}$	$m_{Brz, min}$
1	4	[0 90] <sub>s</sub>	[0.85 0.15]	0.54
	6	[0 0 90] <sub>s</sub>	[0.32 0.53 0.15]	0.54
	8	[0 0 0 90] <sub>s</sub>	[0.29 0.31 0.25 0.15]	0.54
	10	[0 0 0 0 90] <sub>s</sub>	[0.16 0.33 0.15 0.2 0.15]	0.54
2	4	[0 90] <sub>s</sub>	[0.85 0.15]	0.54
	6	[0 0 90] <sub>s</sub>	[0.4 0.45 0.15]	0.54
	8	[0 0 0 90] <sub>s</sub>	[0.032 0.19 0.63 0.15]	0.54
	10	[0 0 0 0 90] <sub>s</sub>	[0.26 0.19 0.2 0.2 0.15]	0.54
3	4	[0 90] <sub>s</sub>	[0.67 0.33]	0.81
	6	[0 0 90] <sub>s</sub>	[0.35 0.32 0.33]	0.81
	8	[0 0 90 90] <sub>s</sub>	[0.25 0.42 0.13 0.2]	0.81
	10	[0 0 0 90 90] <sub>s</sub>	[0.2 0.17 0.3 0.23 0.1]	0.81
4	4	[0 90] <sub>s</sub>	[0.58 0.42]	0.87
	6	[0 0 90] <sub>s</sub>	[0.27 0.31 0.42]	0.87
	8	[0 0 90 90] <sub>s</sub>	[0.34 0.24 0.2 0.22]	0.87
	10	[0 0 0 90 90] <sub>s</sub>	[0.17 0.2 0.21 0.24 0.18]	0.87

assumptions and curtailment of small terms at different stages of development. For optimisation purposes, the value of coefficient does not affect results as the functional dependence on material properties and geometry is identical across authors. The terms  $A_{11}$  and  $D_{22}$  represent the laminate longitudinal extensional and circumferential bending stiffness, respectively.

Considering a design space of symmetric cross-ply laminates, it is reasonable to hypothesise a stacking sequence of [0 90 0] as being optimum for minimising  $M_{Brz}$ . This choice comes about from the following considerations. Firstly,  $A_{11}$  is minimised by 90° and  $D_{22}$  by 0° fibre orientations. Secondly, the effects of 0° and 90° fibre orientations are almost mutually exclusive of each other as there is at least one order magnitude difference between their values of longitudinal stiffness. Finally, whilst  $A_{11}$  is independent of stacking sequence it is noted that  $D_{22}$  is highly stacking sequence dependent so that to minimise  $D_{22}$  requires placing 90° plies at the midplane. Such considerations lead to the hypothesis of a cross-ply laminate with stacking sequence [0 90 0] to be the optimum laminate. This hypothesis is tested by using a numerical minimisation process.

The minimisation process defines the optimum volume fractions of  $n$ -ply symmetric cross-ply symmetric laminates giving the minimum Brazier moment,  $M_{Brz, min}$ , for a circular tube under pure bending for pre-selected materials. Fibre orientation and volume fraction are both optimised in each ply of the laminate for 4, 6, 8 and 10-ply symmetric laminates. Fibre angles are defined as discrete optimisation variables, whereas volume fractions are treated as continuous variables. The minimisation process is applied to four materials, a high-modulus carbon fibre reinforced polymer - material 1, a carbon fibre reinforced polymer - material 2, and two glass fibre reinforced polymers - materials 3 and 4. Table 1 shows their respective material properties.

The objective function is  $\sqrt{A_{11} D_{22}}$  and it is calculated using material invariants and lamination parameters as defined by Tsai and Pagano [22]. The objective function is normalised with respect to the factor  $\frac{t^2}{\sqrt{12}} U_1$ , where  $U_1$  is a material invariant (quasi-isotropic modulus) and  $t$  is



(a) Whole range of examined materials. (b) Selected range of materials for which  $\Delta m_{Brz min} < 5$ .

Fig. 3. Difference in  $m_{Brz min}$  between symmetric cross-ply laminates and 4-ply symmetric laminates for pre-selected materials.

the laminate thickness. The normalisation factor is the equivalent of  $\sqrt{A_{11}D_{22}}$  for a theoretically isotropic material. The normalised objective function is then expressed as

$$m_{Brz} = \frac{\sqrt{12}}{t^2 U_1} \sqrt{A_{11}D_{22}} \quad (2)$$

where the expression for  $A_{11}D_{22}$  is elaborated upon in the next Section (Eq. (11)) and

$$U_1 = \frac{3 E_{11} + E_{22} (3 + 2 \nu_{12}) + 4 G_{12} (1 - \nu_{12} \nu_{21})}{8 (1 - \nu_{12} \nu_{21})} \quad (3)$$

Minimisation is performed using the genetic algorithm optimiser *ga*, within Matlab [23], ensuring a global optimisation. Results are checked through the gradient-based optimiser *fmincon* [23].

Table 2 shows the minimisation results for the four sample materials. The optimum volume fractions of the laminae,  $x_{i opt}$ , and the minimum  $m_{Brz min}$  for 6, 8 and 10-ply laminates show that the optimum 6, 8, 10-ply laminates are equivalent to 4-ply laminates.

These results show that the optimum symmetric cross-ply laminate for the minimisation of  $M_{Brz}$  has stacking sequence [0 90 0] and volume fractions dependent on material properties. This analysis thus confirms our hypothesis for the optimal stacking sequence made in the previous section.

The numerical minimisation was applied to 71 materials with properties in the range  $7 \leq E_{11}/E_{22} \leq 20$ ,  $10.5 \leq E_{11}/G_{12} \leq 42$ ,  $1.5 \leq E_{22}/G_{12} \leq 3$ . The range of material properties is representative of materials with high levels of orthotropy. These materials are interesting because they present relatively small difference in  $m_{Brz min}$  between optimum 4-ply symmetric laminates with negligible extension-shear and bend-twist couplings and optimum symmetric cross-ply laminates. This difference,  $\Delta m_{Brz min}$ , reaches values as little as 1.5% depending on material selection, see Fig. 3a. For materials in the described range, a maximum  $\Delta m_{Brz min}$  of 10% was observed. Fig. 3b shows  $\Delta m_{Brz min}$  for a selection of the examined materials with  $\Delta m_{Brz min} \leq 5\%$ , showing that  $\Delta m_{Brz min}$  is a function of the ratios  $E_{11}/E_{22}$  and  $E_{22}/G_{12}$ .

In the case of materials with smaller orthotropy values, e.g.  $E_{11}/E_{22} \leq 7$ , it could be worthwhile considering the addition of  $\pm 45$ -deg plies for further minimisation of the Brazier moment. However, this is

outside the scope of current work.

### 3. Analytical solution

The previous section verified that [0 90 0] is the optimum stacking sequence for minimising  $M_{Brz}$  considering a design space of symmetric cross-ply laminates. This section presents the analytical solution of the optimum volume fraction of the 90-deg lamina,  $x_{1 opt}$ , of the [0 90 0] laminate as a function of material properties. The solution applies to circular tubes made of arbitrary materials.

The product  $A_{11}D_{22}$  is defined using the transformed stiffness  $\bar{Q}_{11}$ ,  $\bar{Q}_{22}$ .

$$\bar{Q}_{1190} = \bar{Q}_{220} = \bar{Q}_{11} \quad (4)$$

$$\bar{Q}_{2290} = \bar{Q}_{110} = \bar{Q}_{22} \quad (5)$$

where the sub-indexes 0 and 90 refer to 0 and 90-deg plies, respectively.

$$\bar{Q}_{11} = E_{22} / (1 - \nu_{12}\nu_{21}) \quad (6)$$

$$\bar{Q}_{22} = E_{11} / (1 - \nu_{12}\nu_{21}). \quad (7)$$

Then,

$$A_{11} = \bar{Q}_{22}t_{90} + \bar{Q}_{11}(t - t_{90}) \quad (8)$$

$$D_{22} = \frac{1}{12} \left[ \bar{Q}_{11}t_{90}^3 + \bar{Q}_{22}(t^3 - t_{90}^3) \right]. \quad (9)$$

The volume fraction of the 90-deg lamina,  $x_1$ , is defined as

$$x_1 = t_{90}/t. \quad (10)$$

By substituting Eqs. (6) and (7) into Eqs. (8) and (9), the product  $A_{11}D_{22}$  becomes,

$$A_{11}D_{22} = \frac{t^4}{12 (\nu_{12} \nu_{21} - 1)^2} \left( - (E_{11} - E_{22})^2 x_1^4 + E_{11} (E_{11} - E_{22}) x_1^3 - \right) \quad (11)$$

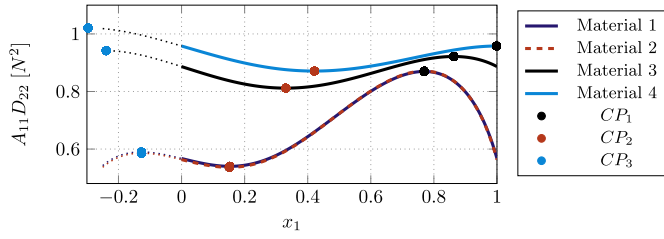


Fig. 4. Evaluation of  $A_{11}D_{22}$  for  $0 < x_1 < 1$  and critical points ( $CP_1$ ,  $CP_2$ ,  $CP_3$ ) for sample materials.

$$E_{22} (E_{11} - E_{22}) x_1 + E_{11} E_{22}$$

And by differentiating Eq. (11) with respect to  $x_1$

$$\frac{d A_{11} D_{22}}{d x_1} = \frac{t^4 (E_{11} - E_{22})}{12 (\nu_{12} \nu_{21} - 1)^2} (-4 (E_{11} - E_{22}) x_1^3 + 3 E_{11} x_1^2 - E_{22}) \quad (12)$$

As such, the three critical points of  $A_{11}D_{22}$ ,  $x_{1,crit\ 1,2,3}$ , are obtained by equating Eq. (12) to zero and solving for  $x_1$

$$x_{1,crit\ 1} = \frac{E_{11}}{4(E_{11} - E_{22})} + \frac{\sqrt[3]{4}}{4} W + \frac{\sqrt[3]{2}}{8} \frac{E_{11}^2}{W(E_{11} - E_{22})^2} \quad (13)$$

$$x_{1,crit\ 2,3} = \frac{E_{11}}{4(E_{11} - E_{22})} - \frac{\sqrt[3]{4}}{8} W \mp \sqrt{3} \left( \frac{\sqrt[3]{4} i}{8} W - \frac{\sqrt[3]{2} i}{16} \frac{E_{11}^2}{W(E_{11} - E_{22})^2} \right) - \quad (14)$$

$$\frac{\sqrt[3]{2}}{16} \frac{E_{11}^2}{W(E_{11} - E_{22})^2}$$

where  $i$  denotes  $\sqrt{-1}$  and with,

$$W = \left( \sqrt{\frac{E_{22} (E_{11}^3 - 4 E_{11}^2 E_{22} + 8 E_{11} E_{22}^2 - 4 E_{22}^3)}{(E_{11} - E_{22})^4}} - \quad (15)$$

$$\frac{2 E_{22}}{E_{11} - E_{22}} + \frac{E_{11}^3}{4 (E_{11} - E_{22})^3} \right)$$

Fig. 4 shows the evaluation of  $A_{11}D_{22}$  in the range  $-0.3 \leq x_1 \leq 1$  including the critical points for four sample materials with properties given in Table 1. Note that  $x_{1,crit\ 1}$  represents the maximum,  $x_{1,crit\ 3}$  lacks physical significance (negative volume fraction) and the minimum  $x_{1,opt}$  corresponds to  $x_{1,crit\ 2}$ . Then,

$$x_{1,opt} = \frac{E_{11}}{4(E_{11} - E_{22})} - \frac{\sqrt[3]{4}}{8} W - \sqrt{3} \left( \frac{\sqrt[3]{4} i}{8} W - \frac{\sqrt[3]{2} i}{16} \frac{E_{11}^2}{W(E_{11} - E_{22})^2} \right) - \quad (16)$$

$$\frac{\sqrt[3]{2}}{16} \frac{E_{11}^2}{W(E_{11} - E_{22})^2}$$

Then, the optimum laminate for minimising the folding load of symmetric cross-ply hinges is [0 90 0] with volume fraction of the 90-

deg layers given by  $x_{1,opt}$ , Eq. (16), which is a function of material properties.

The evaluation of Eq. (16) for 71 materials shows that the imaginary part of the solution,  $Im(x_{1,opt})$ , is negligible compared with the real part of the solution,  $Re(x_{1,opt})$ , see Fig. 5.

### 3.1. Validation

The analytical solution is validated through a parametric FE analysis evaluating the influence of  $x_1$  on the load at which the tube becomes unstable,  $M_i$ , of tubes with stacking sequence [0 90 0]. Results from minimisation, for a given material, are validated if  $x_{1,opt}$  obtained from the analytical solution coincides with the value of  $x_1$  giving the lowest  $M_i$  in the parametric FE analysis. The validation process is presented for material 1.

For each analysed tube a linear buckling analysis (LBA) and a geometrically non-linear static analysis with imperfections (GNIA) using the Riks arc-length algorithm, as implemented in Abaqus [17], are performed. LBAs are performed for perfect tubes to extract the first linear buckling load,  $\lambda_1$ , and its corresponding mode shape which is introduced as a small imperfection in GNIA.  $M_i$  is obtained through GNIA and corresponds to the first nonlinear limit point or bifurcation point.

The tube is modelled in its full length without the use of symmetry using the quadratic shell element S8R5 with element size corresponding to the converged solution of  $\lambda_1$ . Displacements and rotations at both ends of the tube are linked to reference points,  $RP1$  and  $RP2$ , located at the centre of the cross-section, through a kinematic coupling constraint.  $RP1$  and  $RP2$  have all degrees of freedom constrained except from the rotation with respect to the  $x$ -axis and the  $z$ -wise displacement ( $u_x^{RP1,2} = u_y^{RP1,2} = \phi_y^{RP1,2} = \phi_z^{RP1,2} = 0$ ). Bending moments,  $M$ , of same magnitude and opposite sense are applied at the reference points. Additionally, the displacement in  $z$ -direction is constrained at the nodes A and B located at the top and bottom of the mid-span of the tube ( $u_z^{A,B} = 0$ ). LBAs and

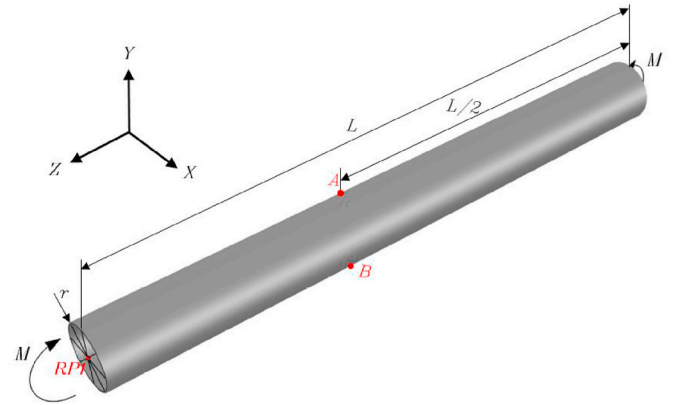


Fig. 6. FE model: Geometry, loads and boundary conditions.

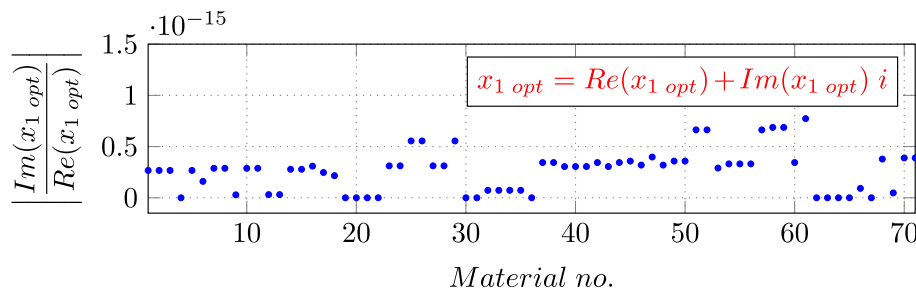


Fig. 5. Ratio of imaginary and real parts of  $x_{1,opt}$  for pre-selected materials.

**Table 3**  
GNIA instability loads,  $M_i$ , for [0 90 0] laminates from material 1.

Laminate	1	2	3	4	5	6	7
$x_1$	0.025	0.05	0.1	0.125	0.15	0.2	0.3
$M_i$ [N·mm] $\times 10^6$	3.54	3.53	3.52	3.51	3.52	3.58	3.80
Laminate	8	9	10	11	12	13	
$x_1$	0.4	0.5	0.6	0.7	0.8	0.9	
$M_i$ [N·mm] $\times 10^6$	4.19	4.63	5.04	5.35	5.44	5.05	

GNIA's share the same boundary conditions, see Fig. 6.

All tubes have  $r = 100\text{ mm}$  and  $t = 1\text{ mm}$ . The length of the tube,  $L = 10\text{ m}$ , was selected after careful FE parametric-length analysis to ensure that boundary conditions have a negligible effect on  $M_i$ . Noting that a 50% increase of this length resulted in less than 2% change of  $M_i$  and  $\lambda_1$ .

The model shows good agreement with the FE results from Rotter et al. [24] which was used as a benchmark.

The analytical solution of  $x_{1\text{ opt}}$ , Eq. (16), delivers  $x_{1\text{ opt}} = 0.15$  for material 1. Table 3 shows  $M_i$  obtained from GNIA for tubes made of material 1 and with different values of  $x_1$ . FE results show that the minimum  $M_i$  corresponds to a tube with  $x_1 = 0.125$ . It is worth noting that for the considered material, tubes with  $x_1 = 0.1, 0.125$  and  $0.15$  present only small differences in  $M_i$  as is expected upon observation of the flatness of the function  $A_{11}D_{22}(x_1)$  in the vicinity of these values of  $x_1$ , see Fig. 4. For both analytical,  $x_1 = 0.15$ , and FE,  $x_1 = 0.125$ , optimum laminates, Fig. 7 shows equilibrium curves obtained from GNIA. The difference in instability moment,  $M_i$ , between these two tubes is only 0.3%. For design purposes, the difference between the analytical and FE solution is negligible.

Moreover, the analytical solution also agrees with results from numerical minimisation data shown in Table 2. It is worth noting that the normalisation factor used for  $m_{B_{rz}}$  in Table 2 solely depends on material properties and the thickness of the laminate, see Eqs. (2) and (3). Therefore, the comparison between  $M_{B_{rz\text{ min}}}$  and its respective normalised value,  $m_{B_{rz\text{ min}}}$ , applies fully for the presented results. The analytical solution also agrees with the parametric FE analysis and numerical optimisation for the rest of sample materials.

Considering computational expense during the design process, the validation study highlights the significance of the analytical solution. The computational cost of one GNIA involves solving a linear static analysis at each iteration of each step of the equilibrium path. Moreover, the computational cost of this process increases with increasing degrees

of freedom that discretise the structural problem. Therefore, an analytical solution for this structural problem can greatly speed up the initial design of these structures.

#### 4. Comparison of analytical solutions of $M_{B_{rz}}$ against FE analysis

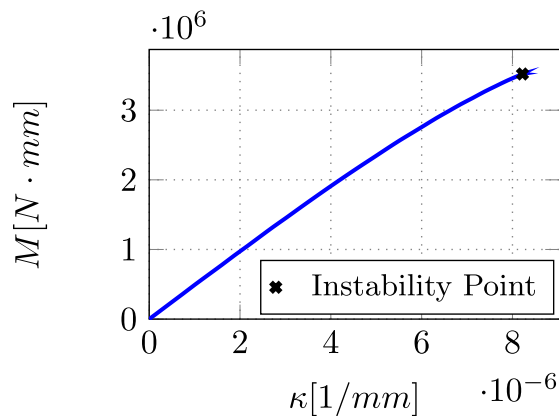
The optimum symmetric cross-ply laminate can be defined based on material properties using the analytical solution presented in Eq. (16). However, the objective function used for minimisation does not deliver the magnitude of  $M_{B_{rz}}$  which is key for design purposes.  $M_{B_{rz}}$  can be predicted analytically according to a number of available solutions.

Geometrically nonlinear FE analysis employs fewer assumptions than available analytical solutions but has high computational cost. A comparison of FE against analytical solutions can help the designer in the choice of analytical solution for preliminary design.

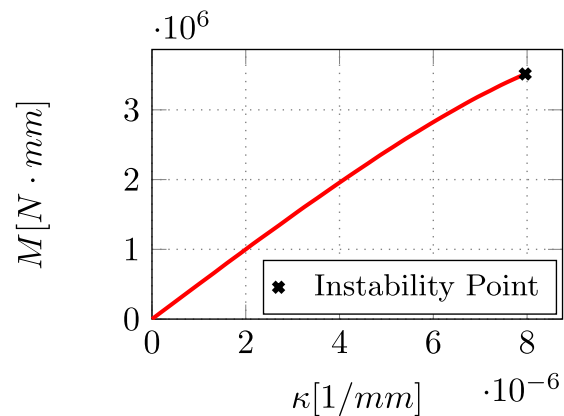
The results for 36 tubes with stacking sequence [0 90 0] and different values of  $x_1$  are presented. For these tubes, Figs. 8 and 9 show  $M_i$  against the analytical solutions of  $M_{B_{rz}}$  from Stockwell and Cooper [19],  $M_{B_{rz}}^S$ ; Harursampath and Hodges [20],  $M_{B_{rz}}^H$ ; Tatting et al. [21],  $M_{B_{rz}}^T$ ; and Kedward [18],  $M_{B_{rz}}^K$  for materials 1, 2, 3 and 4. All of the considered analytical solutions are applicable to cross-ply laminates. FE results fit best with the analytical solution proposed by Stockwell and Cooper [19] for all examined tubes. A difference of 6% is observed between  $M_i$  and  $M_{B_{rz}}^S$  for the optimum laminates made of materials 1 and 2. Materials 3 and 4 show less than 1% difference between  $M_i$  and  $M_{B_{rz}}^S$  for the optimum laminates.

#### 5. Investigation of critical instability

Analytical solutions of  $M_{B_{rz}}$  consider that structures only become unstable due to the Brazier instability. In contrast, GNIA also considers local buckling which can occur due to compressive stress and which could precede Brazier instability. This Section investigates whether the examined tubes become unstable due to Brazier instability or local buckling. This prediction is important for a successful folding process that exploits the Brazier moment. In fact, the equilibrium path of a circular tube exhibiting Brazier instability is smooth in both its stable and unstable regions, see Fig. 2. This means that the structure can gradually fold with increasing load. Instead, the equilibrium path of a circular tube exhibiting local instability is smooth and stable up to  $M_i$ . Then, the post-critical branch is highly unstable. The structure exhibits a sudden change of shape with associated dynamic effects and localised stresses that, if not appropriately considered, can compromise the success of the folding process.

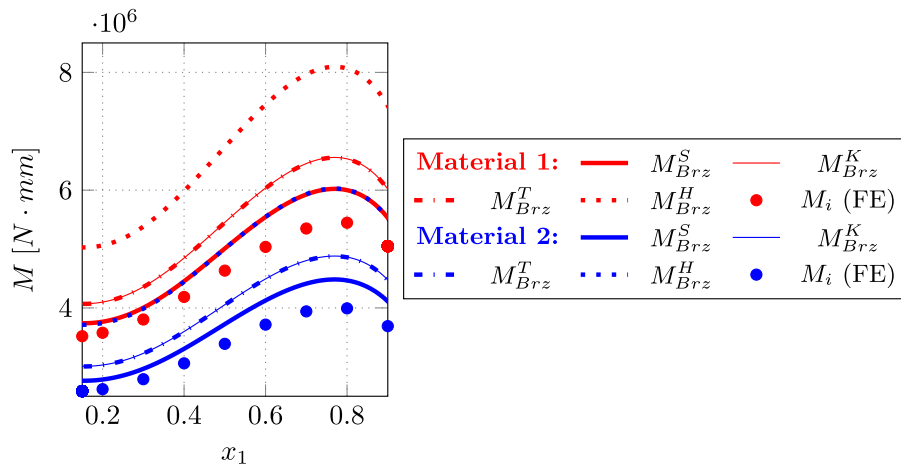


(a) Optimum from analytical solution,  $x_1 = 0.15$ .

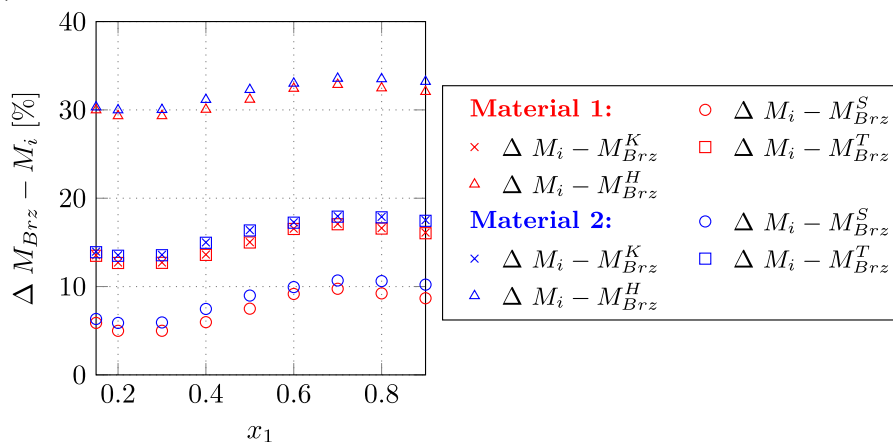


(b) Optimum from FE analysis,  $x_1 = 0.125$ .

Fig. 7. Moment-curvature ( $M, \kappa$ ) equilibrium curve for analytical and FE optimum laminates for material 1.



(a) Analytical solutions of  $M_{Brz}$  and FE instability load,  $M_i$



(b) Percentage difference between analytical solutions of  $M_{Brz}$  and  $M_i$

Fig. 8. Analytical solutions of  $M_{Brz}$  against FE instability load,  $M_i$ , for tubes made of carbon fibre reinforced polymers, materials 1 and 2.

Tatting et al. [21] defined the parameter,  $\chi$ , for the prediction of the critical instability as

$$\chi = \sqrt{\frac{D_{11}E_\theta}{D_{22}E_z}} \quad (17)$$

where

$$E_\theta = \frac{A_{11}A_{22} - A_{12}^2}{A_{22}t} \quad (18)$$

$$E_z = \frac{A_{11}A_{22} - A_{12}^2}{A_{11}t} \quad (19)$$

The term  $\chi$  applies to laminates with negligible extension-shear and bend-twist couplings and is a ratio of the stiffnesses critical to local buckling,  $D_{11}E_\theta$ , and the stiffnesses critical to the Brazier instability,  $D_{22}E_z$ . Tubes with high values of  $\chi$  are more likely to reach instability due to Brazier phenomena. While tubes with low values of  $\chi$  become unstable by local buckling instability.

Fig. 10 shows the evaluation of  $\chi$  for laminates made of the sample materials with  $0 \leq x_1 \leq 1$ . The role of material orthotropy in the problem becomes evident in Fig. 10 since material 1 and 2, having only a small difference in  $E_{11}/E_{22}$  (17.6 and 18, respectively), present almost

identical values of  $\chi$ .

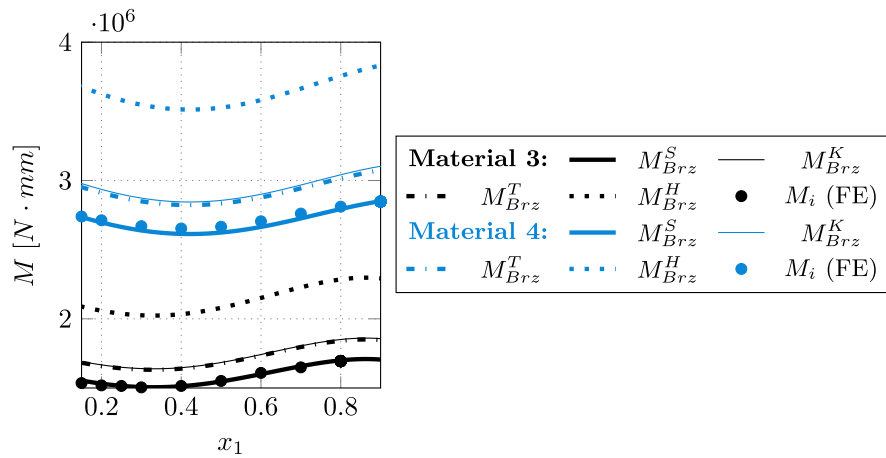
Fig. 11 shows an example of the influence of  $\chi$ . It shows GNIA equilibrium curves of two tubes, tube A and B, made from material 1 and having the same geometry ( $L = 10$  m,  $r = 100$  mm,  $t = 1$  mm) but different values of  $\chi$ . The layup of tube A is  $[0\ 90\ 0]$  with 62% of 90-deg plies, having  $\chi = 2.1$ . While the layup of tube B is  $[90\ 0\ 90]$  with 62% of 0-deg plies, having  $\chi = 0.5$ . Fig. 11a shows the moment-curvature curve while Fig. 11b shows the moment - cross-sectional flattening relationship. The cross-sectional flattening,  $\zeta$ , and curvature,  $\kappa$ , are calculated as

$$\zeta = \frac{d - d_0}{d_0} \quad (20)$$

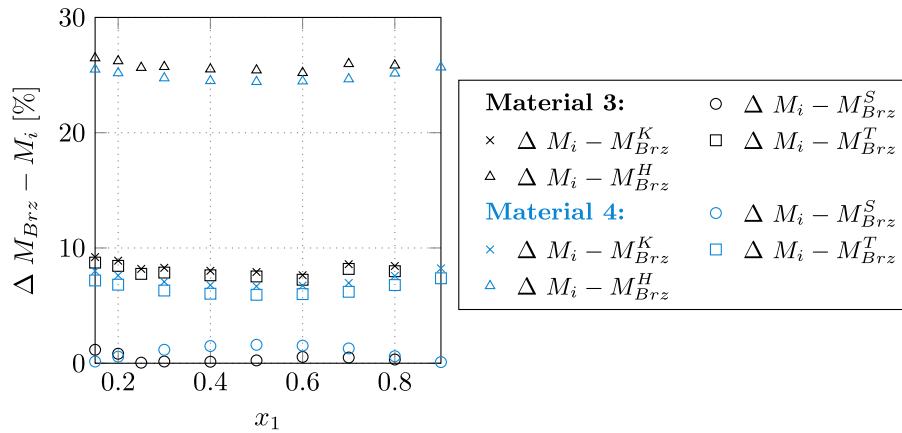
$$\kappa = \frac{2\phi_x}{L_0} \quad (21)$$

where  $d$  is the tube diameter, the subindex 0 denotes the undeformed geometry of the tube and  $\zeta$  is evaluated at the mid-span of the tube.

Tube A exhibits a more pronounced nonlinear pre-critical behaviour than tube B due to larger  $\zeta$ . The instability load,  $M_i$ , of tube A is 9.3% smaller than  $M_{Brz}^S$ . In contrast, tube B exhibits a value of  $M_i$  that is 44.7% smaller than  $M_{Brz}^S$ . The non-pronounced cross-sectional flattening of tube B and the large difference between  $M_{Brz}^S$  and  $M_i$  observed for tube B



(a) Analytical solutions of  $M_{Brz}$  and FE instability load,  $M_i$ .



(b) Percentage difference between analytical solutions of  $M_{Brz}$  and  $M_i$ .

Fig. 9. Analytical solutions of  $M_{Brz}$  against FE instability load,  $M_i$ , for tubes made of glass fibre reinforced polymer, materials 3 and 4.

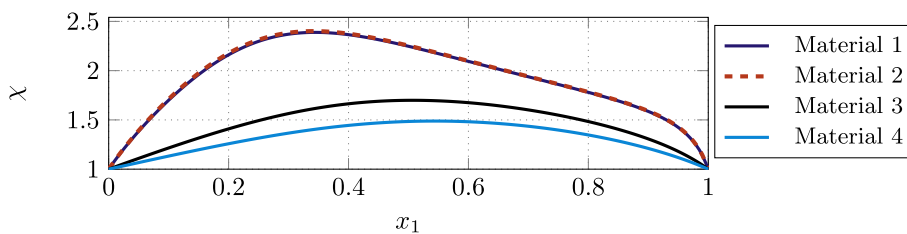


Fig. 10. Evaluation of  $\chi$  for [0 90 0] laminates made of materials 1, 2, 3 and 4.

suggests that local buckling precedes Brazier instability for this tube. Additional LBA analyses were performed for both tubes to assess this possibility. The cross-section of the tube used in the LBA is an elliptical approximation of the deformed mid-span cross-section at the moment the tube becomes unstable in the GNIA, see Fig. 12. The length of the minor axis of the ellipse equals the distance between the highest and lowest points of the midspan deformed cross-section at the moment when instability occurs. The elliptical approximation of the cross-section ensures the consideration of the pre-critical cross-sectional flattening. Neglecting the pre-critical deformation of the tube by considering the initial undeformed circular cross-section for the LBA significantly overestimates the buckling load of the tube because the LBA is based on a linearised eigenvalue algorithm. The first buckling load is  $\lambda_1^e$ . Fig. 13 shows the respective buckling mode for half-span of tubes A and B, the

mode is symmetric with respect to the plane passing through the mid-span and parallel to the plane  $xy$ . Additionally, Tatting et al. [21] prediction of the local bifurcation moment,  $\lambda_1^T$ , is calculated. The prediction of  $\lambda_1^T$  is based on Seide and Weingarten's [25] assumption which states that the critical local buckling stress of a tube under bending can be approximated with the critical buckling stress of a tube under axial compression. Note, the radius of the tube under compression corresponds to the largest radius of curvature of the deformed cross-section of the tube under bending at the instability moment.

$M_i$  of tube B is only 1.5% less than  $\lambda_1^e$ . The behaviour of this tube is not representative of Brazier instability, it becomes unstable by local buckling.

Fig. 14 shows a comparison of the axial component stress contour

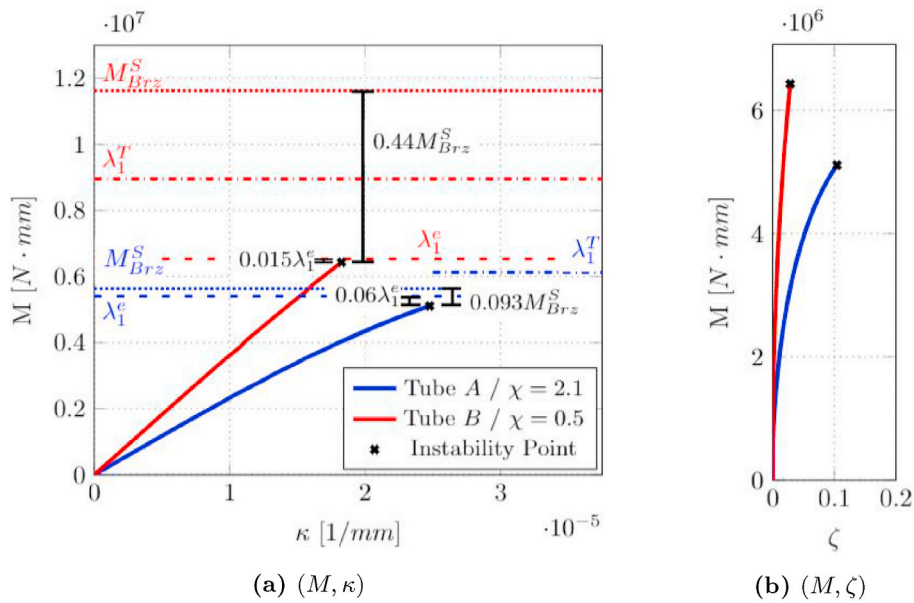


Fig. 11. Equilibrium curves of two tubes made of material 1 with different values of  $\chi$ .

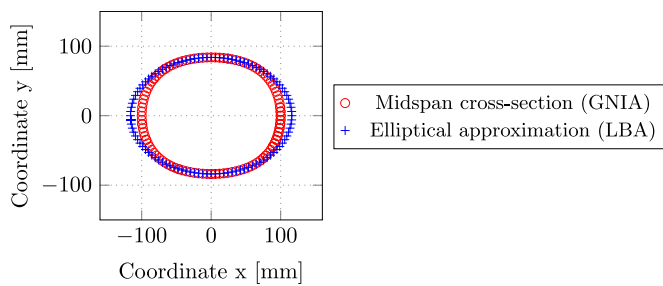


Fig. 12. Midspan cross-section at instability point from GNIA and elliptical cross-section approximation used for LBA.

plots for half-span of tubes A and B at the instability moment in GNIA and the deformed mid-span cross-section when instability occurs. Tube B shows localised peak stresses characteristic of local buckling on the

compressive side of the tube and little flattening compared to tube A.

An analogous comparison to that shown in Fig. 11 is shown in Fig. 15 for material 4 - glass fibre reinforced polymer. In this case Tube C has stacking sequence [0 90 0] and 60% of 90-deg plies with  $\chi = 1.5$ . Tube D has stacking sequence [90 0 90] and 60% of 0-deg plies with  $\chi = 0.7$ . Note that tube C reaches the highest degree of flattening compared to tubes A, B and D and it is also the tube reaching instability closest to its prediction of  $M_{Brz}^S$ , exhibiting only 2% difference between  $M_{Brz}^S$  and  $M_i$ . Material 4 is less stiff than material 1, therefore, the ovalisation characteristic of Brazier instability is expected to be more pronounced as results show, see Fig. 15b. Analogous to tube B, tube D exhibits less critical nonlinear behaviour than tube C. As well as for tube D,  $\lambda_1^e$  and  $\lambda_1^T$  are smaller than  $M_{Brz}^S$  and closer to  $M_i$ . Tube D is more likely to reach instability due to local buckling.

All observations made in this section support the results of Tatting et al. regarding  $\chi$ . As such, large values of  $\chi$  represent structures more likely to become unstable due to Brazier instability, i.e. cross-sectional

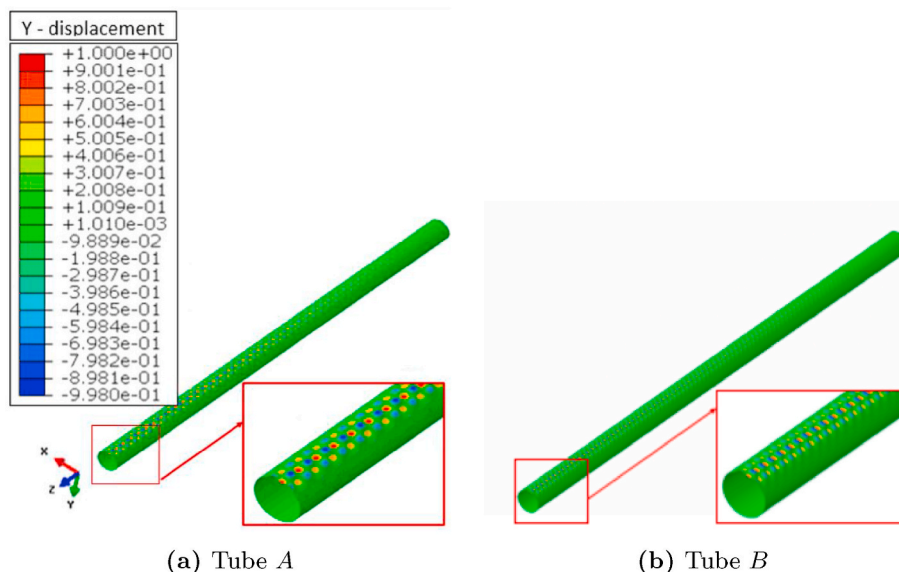


Fig. 13. 1<sup>st</sup> buckling mode (local buckling) for half-span of tubes A and B (elliptical approximation cross-section).

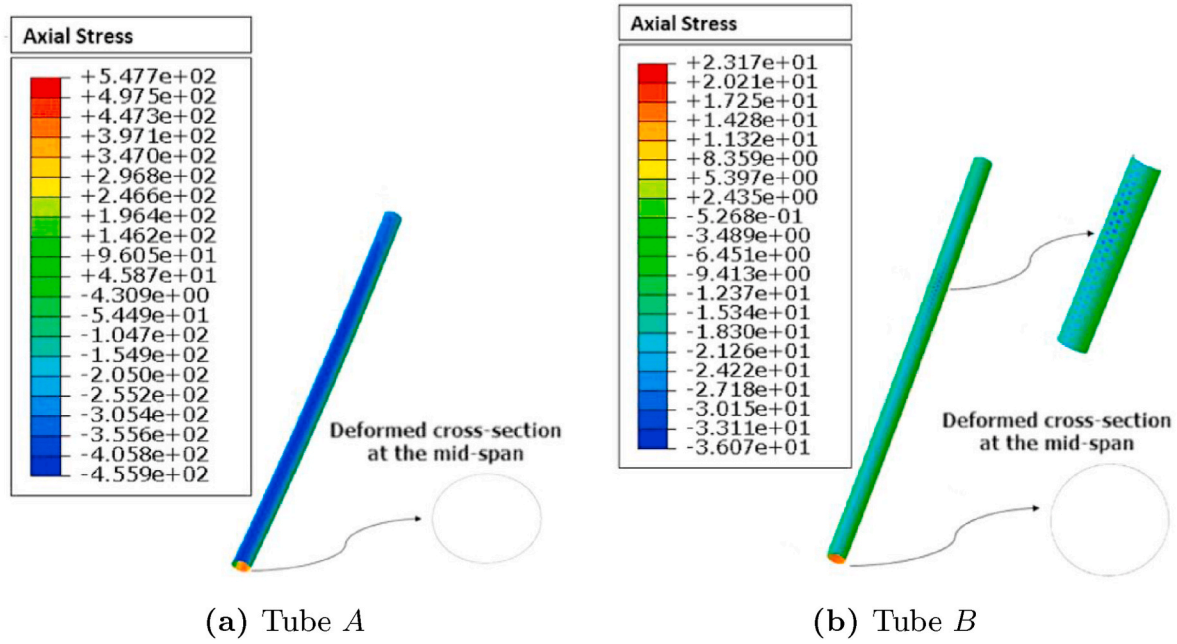


Fig. 14. Axial component stress contour plot at instability moment for half-span of tubes A and B.

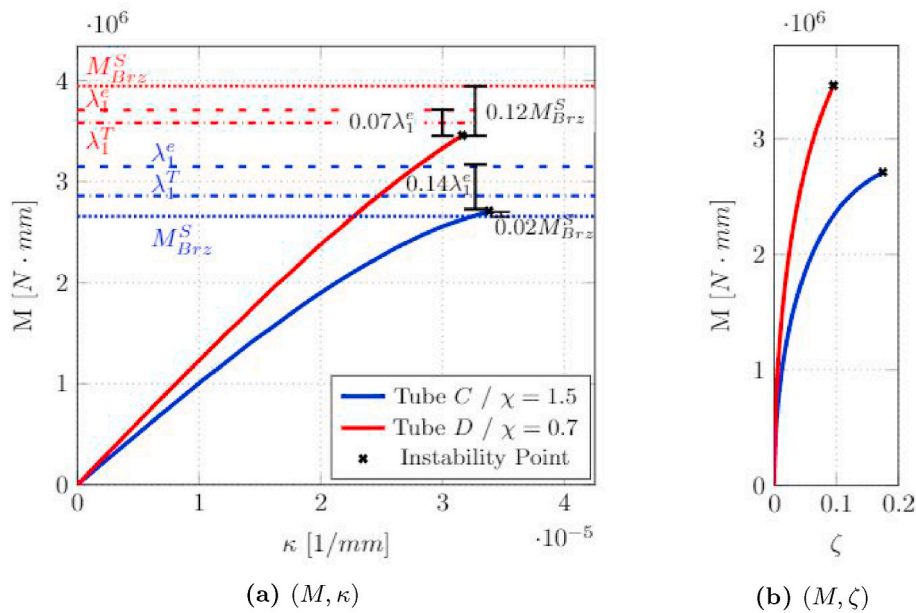


Fig. 15. Equilibrium curves of two tubes made of material 4 with different values of  $\chi$ .

ovalisation, while small values of  $\chi$  represent structures (e.g. tubes B and D) that are more likely to become unstable due to local buckling. Tatting et al. [21] present results comparing the instability points of both instabilities for tubes with  $0 < \chi < 4$ . Fig. 16 presents the comparison of the instability loads of the two instability types for laminates with  $0 \leq \chi \leq 3$  as defined by Tatting et al. In this figure, the normalised Brazier limit moment,  $m_{Brz}^T$ , and the normalised bifurcation local buckling moment,  $\bar{\lambda}_1^T$ , are calculated according to Tatting et al. [21]. Additionally, this plot includes the normalised Brazier limit moment according to Stockwell and Cooper,  $m_{Brz}^S$ , since our results show it gives the most accurate prediction, see Section 4. Moreover, for tubes made of materials 1, 2, 3 and 4, with stacking sequence [0 90 0] and different values of  $x_1$ , this plot includes the normalised instability moment from GNIA,  $m_i$ ,

and the normalised bifurcation local buckling moment from LBA,  $\bar{\lambda}_1^e$ . All moments are normalised as per Tatting et al. [21] using the classical buckling moment of an infinite tube under axial compression,

$$\lambda_{cl} = 2\pi r \sqrt{D_{11} E_{\theta t}} \quad (22)$$

Fig. 16 shows how the two instability loads are similarly valued for larger values of  $\chi$  which correspond to carbon fibre reinforced laminates, while glass-fibre reinforced laminates have larger differences between instability loads. Moreover, laminates made of glass fibre reinforced polymer have small differences between their instability load from GNIA,  $M_i$ , and the prediction  $M_{Brz}^S$ . Laminates made from materials 3 and 4 are more likely to reach instability due to Brazier instability.

On the other hand, for laminates made of materials 1 and 2 the instability points for local buckling and Brazier instability are highly

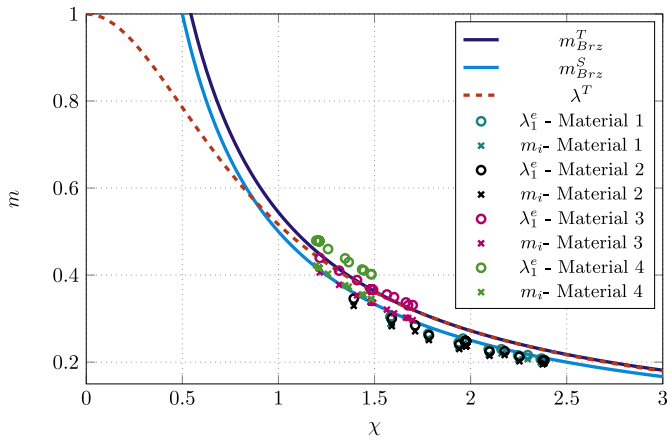


Fig. 16. Evaluation of  $m_{Brz}^T$ ,  $m_{Brz}^S$ ,  $\lambda^T$ ,  $\lambda_1^e$ ,  $m_i$  for laminates with  $0 \leq \chi \leq 3$ .

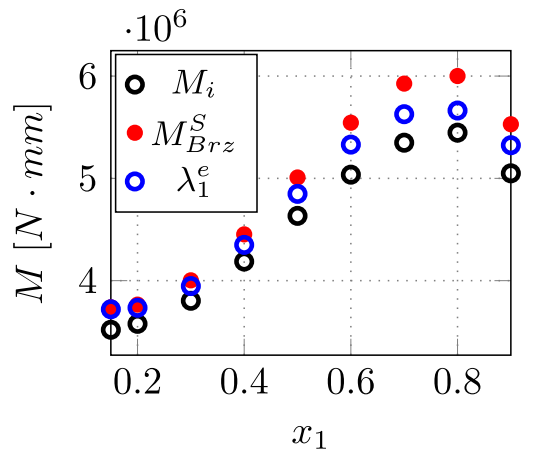
similar, making it troublesome for the prediction of the instability mode more likely to happen first. An investigation to determine which is the critical instability for these tubes follows.

Local buckling was studied numerically through LBA using straight tubes having an elliptical cross-section which approximates the

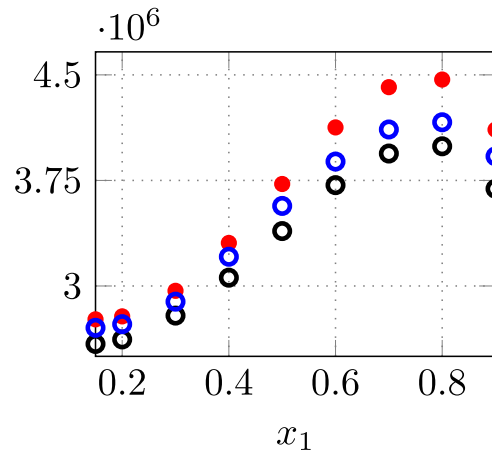
deformed midspan cross-section at the moment of instability in GNIA, see Fig. 12. In parallel, the Brazier instability was identified using Stockwell and Cooper’s analytical solution [19]. Then  $M_i$  is compared against  $\lambda_1^e$  and  $M_{Brz}^S$  to identify the type of instability. Fig. 17 shows, for tubes with different values of  $x_1$  and made of sample materials 1 and 2, a comparison of  $M_i$ ,  $M_{Brz}^S$  and  $\lambda_1^e$ . Also results for materials 3 and 4 are presented to illustrate the contrast between the behaviour of the carbon-fibre reinforced material and glass fibre-reinforced material.

Results presented in Fig. 17 suggest that the majority of tubes made of materials 1 and 2 reach instability due to local buckling before  $M_{Brz}$  is reached. However, it must be noted that the GNIA model includes a small geometrical imperfection corresponding to the first buckling mode, i.e. local buckling. Cylinders are known to be imperfection sensitive structures. There are relatively few papers on imperfection sensitivity of cylinders under bending. Fajuyitan et al. [26,27] studied the imperfection sensitivity of isotropic tubes under bending. To the best of the authors’ knowledge, no studies dedicated to imperfection sensitivity of orthotropic cylinders under bending are available, so further information relevant for purposes can be gleaned.

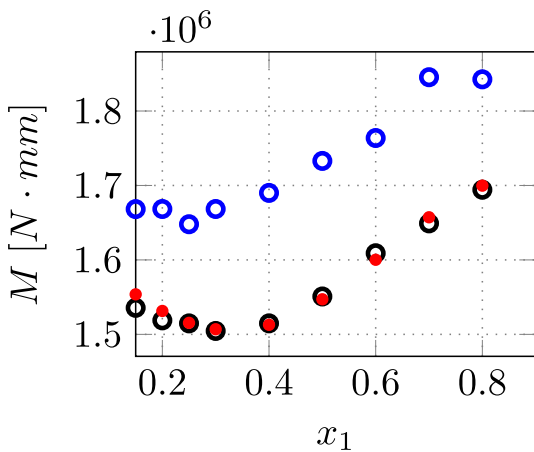
To assess the influence of the original imperfection used in the model (*imperfection type 1*) on the critical instability, GNIA were performed using different imperfections. The new imperfection type (*imperfection type 2*) is a mesh perturbation at the midspan of the tensile side of the



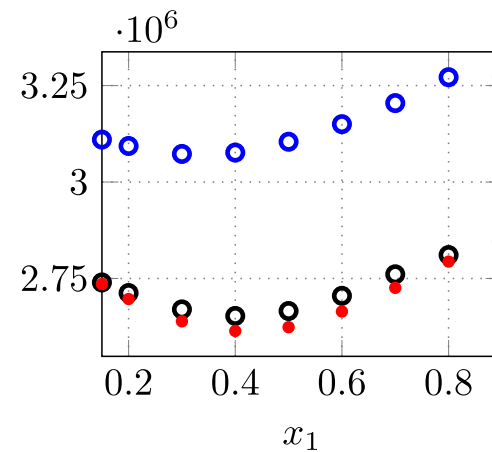
(a) Material 1



(b) Material 2



(c) Material 3



(d) Material 4

Fig. 17. Comparison of  $M_i$ ,  $M_{Brz}^S$  and  $\lambda_1^e$ .

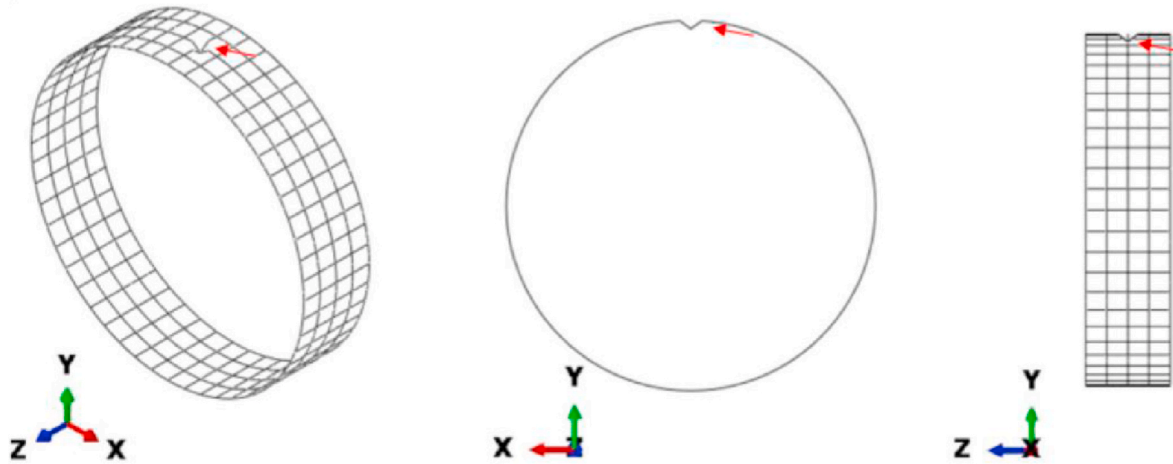


Fig. 18. Mid-span tube section showing imperfection type 2.

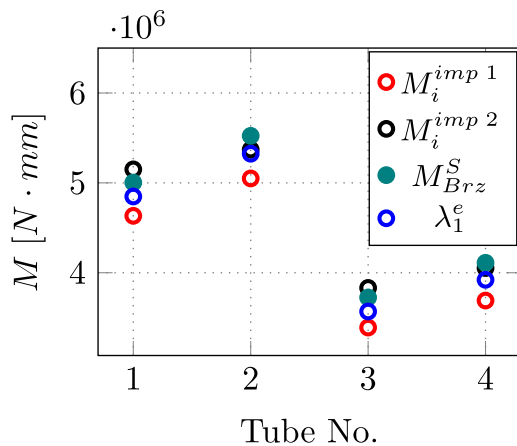
Table 4

Tubes examined for the assessment of the influence of imperfection type on the instability load,  $M_i$ .

Tube	1	2	3	4
Material	1	1	2	2
$x_1$	0.5	0.9	0.5	0.9

tube achieved by offsetting the corresponding node towards the neutral plane of the tube, see Fig. 18. The location of the mesh perturbation in the tensile side of the tube avoids the potential enforcement of local buckling and slightly flattens the cross-section locally. A comparison of these imperfection types was performed for four tubes with geometry and material given in Table 4. All tubes have stacking sequence [0 90 0].

Fig. 19a shows  $M_i^{imp 1}$ ,  $M_i^{imp 2}$ ,  $M_{Brz}^S$  and  $\lambda_1^e$  for tubes 1, 2, 3 and 4. For these tubes,  $M_i^{imp 2}$ ,  $M_i^{imp 1}$ . Fig. 19b presents the percentage difference between  $M_i^{imp 1}$  and  $M_i^{imp 2}$  against  $M_{Brz}^S$ .  $M_i^{imp 2}$  present a difference against  $M_{Brz}^S$  of between 1.4% and 3.1%. While the range of difference of  $M_i^{imp 1}$  and  $M_{Brz}^S$  is between 5.6% and 10.2%. Results show that tubes with imperfection type 2 become unstable at a load higher than the critical load for local buckling instability and closer to the prediction of  $M_{Brz}$  according to Stockwell and Cooper.



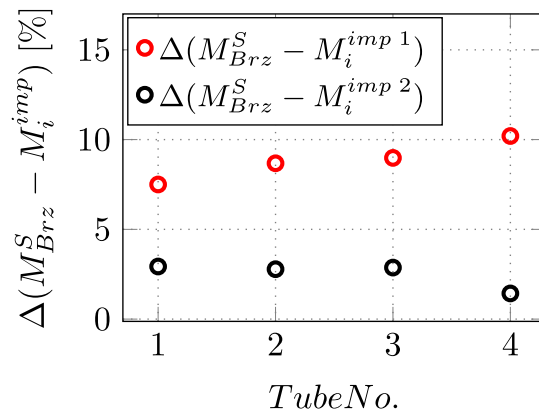
(a) Comparison of  $M_i^{imp 1}$ ,  $M_i^{imp 2}$ ,  $M_{Brz}^S$  and  $\lambda_1^e$ .

Our analysis suggests that for tubes with large values of  $\chi$ , where the instability loads of Brazier instability and local buckling almost coincide, the type of imperfection present in the tube favours the tube to become unstable by the instability corresponding to that imperfection. This consideration could constitute an additional degree of freedom in design, especially when real structures are considered. The prediction of the critical instability for tubes with large values of  $\chi$  is troublesome for practical purposes. For these tubes, if it is desired that they become unstable specifically due to the Brazier instability, the Brazier instability could be induced enforcing the ovalisation of the cross-section by external means, e.g. external pressure, adequate imperfections.

### 6. Conclusions

An analytical solution of the optimum laminate for the minimisation of the folding load of flexible hinges made of symmetric cross-ply laminates of arbitrary materials has been presented. The solution shows that the optimum laminate has stacking sequence [0 90 0] and its volume fraction is an algebraic function of material orthotropy. Good agreement was found between the analytical solution, geometrically nonlinear FE analysis and numerical minimisation.

Flexible hinges made of symmetric cross-ply laminates using materials with high levels of orthotropy prove to be interesting since their



(b) Percentage difference between  $M_i^{imp 1}$ ,  $M_i^{imp 2}$  and  $M_{Brz}^S$ .

Fig. 19. Results comparison for imperfection types 1 and 2.

difference in minimum Brazier moment, i.e. folding load, can be as little as 1.5 % against generic 4-ply symmetric laminates with negligible extension-shear and bend-twist couplings.

With the aim of assisting the designer in the prediction of folding loads during preliminary design, a comparison of analytical solutions against FE analysis was offered. The analytical solution from Stockwell and Cooper [19] fits best with FE results and is so recommended for preliminary design, showing a maximum difference of 6% against FE results for the optimum laminates. Additionally, insights on the prediction of the instability mode most likely to initially take place for the examined tubes, i.e. Brazier instability or local buckling instability, were provided. The parameter,  $\chi$ , proposed by Tatting et al. [21] for the prediction of the instability mechanism was considered. For tubes with stacking sequence [0 90 0], the parameter showed itself to be of practical importance for small values - i.e. tubes made of glass fibre reinforced polymer. For larger values of  $\chi$ , which represents carbon fibre reinforced polymer, the close proximity of instability points complicates the use of the parameter for prediction purposes. However, geometrically nonlinear FE analysis showed that the desired instability could be enforced by superposing a deformation corresponding to the desired instability. In fact, the four scrutinised tubes with an imperfection characteristic of Brazier instability presented a range of differences between 1.4 and 3.1%. reflecting the range between the instability load from geometrically nonlinear FE analysis and the prediction of Brazier moment according to Stockwell and Cooper [19]. The possibility of controlling the instability type occurring during folding is of particular interest to influence post-critical behaviour, i.e. the behaviour of the structure while folding occurs.

#### Declaration of competing interest

The authors declare that they have no known competing financial interests or personal relationships that could have appeared to influence the work reported in this paper.

#### Acknowledgments

The authors would like to thank Science Foundation Ireland for funding the Spatially and Temporally Variable Composite Structures grant no. (15/RP/2773) under its Research Professor program.

#### References

- [1] C. Dawson, J. Vincent, A.-M. Rocca, How pine cones open, *Nature* 390 (1997), <https://doi.org/10.1038/37745>.
- [2] S. Barbarino, O. Bilgen, R.M. Ajaj, M.I. Friswell, D.J. Inman, A review of morphing aircraft, *J. Intell. Mater. Syst. Struct.* 22 (9) (2011) 823–877, <https://doi.org/10.1177/1045389X11414084>.
- [3] S. Daynes, P.M. Weaver, Review of shape-morphing automobile structures: concepts and outlook, *Proc. Inst. Mech. Eng. - Part D J. Automob. Eng.* 227 (11) (2013) 1603–1622, <https://doi.org/10.1177/0954407013496557>.
- [4] X. Lachenal, S. Daynes, P.M. Weaver, Review of morphing concepts and materials for wind turbine blade applications, *Wind Energy* 16 (2) (2013) 283–307, <https://doi.org/10.1002/we.531>.
- [5] G.E. Fenci, N.G. Currie, Deployable structures classification: a review, *Int. J. Space Struct.* 32 (2) (2017) 112–130, <https://doi.org/10.1177/0266351117711290>.
- [6] D.S. Adams, M. Mobrem, Analysis of the lenticular jointed MARSIS antenna deployment, in: 47th AIAA/ASME/ASCE/AHS/ASC Structures Structural Dynamics and Materials Conference, 2006, pp. 1–13.
- [7] J.C. Yee, S. Pellegrino, Composite tube hinges, *J. Aero. Eng.* 18 (4) (2005) 224–231, [https://doi.org/10.1061/\(ASCE\)0893-1321](https://doi.org/10.1061/(ASCE)0893-1321).
- [8] H.M.Y.C. Mallikarachi, S. Pellegrino, Quasi-static folding and deployment of ultrathin composite tape-spring hinges, *J. Spacecraft Rockets* 48 (1) (2011) 187–198, <https://doi.org/10.2514/1.47321>, oi:10.2514/1.47321. URL <https://doi.org/10.2514/1.47321>.
- [9] X. Lachenal, P. Weaver, A. Pirrera, Concept for a deployable wing, in: ASME 2014 Conference on Smart Materials, Adaptive Structures and Intelligent Systems, SMASIS, vol. 2, 2014, <https://doi.org/10.1115/SMASIS2014-7428>.
- [10] T. Von KärmÄjn, Ueber die formänderung dünnwandiger rohre, insbesondere federrnder ausgleichrohre, *Z. VDI* 55 (1911) 1889–1895.
- [11] L.G. Brazier, On the flexure of thin cylindrical shells and other "thin" sections, *Proc. Roy. Soc. Lond. A* 116 (1927) 104–114, <https://doi.org/10.1098/rspa.1927.0125>.
- [12] A. G. Bowen P, G. Zucco, P. M. Weaver, Orthotropic cylindrical flexible hinges by exploiting nonlinear brazier phenomena, Submitted to AIAA J..
- [13] L.S. Cecchini, P.M. Weaver, Optimal fiber angles to resist the brazier effect in orthotropic tubes, *AIAA J.* 40 (10) (2002) 2136–2138, <https://doi.org/10.2514/2.1551>.
- [14] C. Mallikarachi, S. Pellegrino, Optimized Designs of Composite Booms with Tape Spring Hinges, 2010, <https://doi.org/10.2514/6.2010-2750>.
- [15] F. Jensen, P. Weaver, L. Cecchini, H. Stang, R. Nielsen, The brazier effect in wind turbine blades and its influence on design, *Wind Energy* 15 (2) (2012) 319–333, <https://doi.org/10.1002/we.473>. <https://onlinelibrary.wiley.com/doi/pdf/10.1002/we.473>.
- [16] L.S. Cecchini, P.M. Weaver, Brazier effect in multibay airfoil sections, *AIAA J.* 43 (10) (2005) 2252–2258, <https://doi.org/10.2514/1.11736>. :10.2514/1.11736. URL <https://doi.org/10.2514/1.11736>.
- [17] ABAQUS/Standard User's Manual, Dassault Systemes Simulia Corp, United States, 2017.
- [18] K. Kedward, Nonlinear Collapse of Thin-Walled Composite Cylinders under Flexural Loading, Proc., 2nd. Internat. Conference on Composite Materials, Metallurgical Society of AIME, Warrendale, 1999, [https://doi.org/10.1016/S0020-7462\(98\)00070-5](https://doi.org/10.1016/S0020-7462(98)00070-5).
- [19] A. Stockwell, P. Cooper, Collapse of Composite Tubes under End Moments, 1992, pp. 1841–1850, <https://doi.org/10.2514/6.1992-2389>.
- [20] D. Harusampath, D.H. Hodges, Asymptotic analysis of the non-linear behavior of long anisotropic tubes, *Int. J. Non Lin. Mech.* 34 (6) (1999) 1003–1018, [https://doi.org/10.1016/S0020-7462\(98\)00070-5](https://doi.org/10.1016/S0020-7462(98)00070-5).
- [21] B.F. Tatting, Z. Guerdal, V.V. Vasiliev, Nonlinear response of long orthotropic tubes under bending including the brazier effect, *AIAA J.* 34 (9) (1996) 1934–1940, <https://doi.org/10.2514/3.13328>.
- [22] S. Tsai, N.J. Pagano, *Invariant Properties of Composite Materials*, 1968.
- [23] *Matlab Optimization Toolbox, the MathWorks, Natick, MA, USA, 2018.*
- [24] J.M. Rotter, A.J. Sadowski, L. Chen, Nonlinear stability of thin elastic cylinders of different length under global bending, *Int. J. Solid Struct.* 51 (15) (2014) 2826–2839, <https://doi.org/10.1016/j.ijsolstr.2014.04.002>.
- [25] P. Seide, V.I. Weingarten, On the buckling of circular cylindrical shells under pure bending, *J. Appl. Mech.* 28 (1) (1961) 112–116, <https://doi.org/10.1115/1.3640420>.
- [26] O. Fajuyitan, A. Sadowski, J. Rotter, A study of imperfect cylindrical steel tubes under global bending and varying support conditions, in: Proc. of 8th Intl. Conf. on Advances in Steel Structures, 2015, <https://doi.org/10.13140/RG.2.1.4642.4403>.
- [27] O.K. Fajuyitan, A.J. Sadowski, Imperfection sensitivity in cylindrical shells under uniform bending, *Adv. Struct. Eng.* 21 (16) (2018) 2433–2453, <https://doi.org/10.1177/1369433218804928>, doi:10.1177/1369433218804928. URL <https://doi.org/10.1177/1369433218804928>.